

1 **High-resolution (1 km) Polar WRF output for 79°N Glacier and the Northeast of Greenland**  
2 **from 2014-2018**

3  
4 Jenny V. Turton<sup>1</sup>, Thomas Mölg<sup>1</sup>, Emily Collier<sup>1</sup>

5 <sup>1</sup>Climate System Research Group, Institute of Geography, Friedrich-Alexander University, Erlangen-  
6 Nürnberg, 90158, Germany.

7  
8 *Correspondence to:* Jenny V. Turton ([jenny.turton@fau.de](mailto:jenny.turton@fau.de))

9  
10 **Abstract**

11 **The northeast region of Greenland is of growing interest due to changes taking place on the**  
12 **large marine-terminating glaciers which drain the north east Greenland ice stream.**  
13 **Nioghalvfjerdingsfjorden, or 79°N Glacier, is one of these that is currently experiencing**  
14 **accelerated thinning, retreat and enhanced surface melt. Understanding both the influence of**  
15 **atmospheric processes on the glacier and feedbacks from changing surface conditions is crucial**  
16 **for our understanding of present stability and future change. However, relatively few studies**  
17 **have focused on the atmospheric processes in this region, and even fewer have used high-**  
18 **resolution modelling as a tool to address these research questions. Here we present a high**  
19 **spatial- (1 km) and temporal- (up to hourly) resolution atmospheric modelling dataset,**  
20 **NEGIS\_WRF, for the 79°N and northeast Greenland region from 2014-2018, and an evaluation**  
21 **of the model's success at representing daily near-surface meteorology when compared with**  
22 **automatic weather station records. The dataset, (Turton et al, 2019b:**  
23 **[doi.org/10.17605/OSF.IO/53E6Z](https://doi.org/10.17605/OSF.IO/53E6Z)), is now available for a wide variety of applications in the**  
24 **atmospheric, hydrological and oceanic sciences in the study region.**

25  
26 **1. Introduction**

27 The surface mass balance of a glacier is largely controlled by regional climate through varying mass  
28 gains and losses in the ablation and accumulation zones, respectively. The large amount of mass lost  
29 from the Greenland Ice Sheet (GrIS) within the last few decades (approximately 3800 billion tonnes of  
30 ice between 1992 and 2018: Shepherd et al., 2020) has largely been located around the coast of  
31 Greenland, due to the thinning and retreat of marine-terminating glaciers (Howat & Eddy, 2011), and  
32 the surface mass loss in the ablation zone due to enhanced melting and runoff (Rignot, et al., 2015;  
33 van den Broeke et al., 2017). A recent study found that enhanced meltwater run off, connected to  
34 changing atmospheric conditions, was the largest contributor of mass loss for Greenland (52%)  
35 (Shepherd et al., 2020). The remaining 48% of mass loss (1.8 billion tonnes of ice) was due to  
36 enhanced glacier discharge, which has been increasing over time (Shepherd et al., 2020).

37           The majority of studies of the surface mass loss in Greenland and its atmospheric controls are  
38 largely constrained to southern and western Greenland (e.g Kuipers Munneke et al., 2018; Mernild et  
39 al., 2018), or to specific warm events such as the 2012 melt event (e.g Bennartz et al., 2013; Tedesco  
40 et al., 2013). However, recent studies have shown that the northeast of Greenland, specifically the  
41 North East Greenland Ice Stream (NEGIS) is now experiencing high ice velocity and accelerated  
42 thinning rates (Joughin et al., 2010; Khan et al., 2014). NEGIS extends into the interior of the  
43 Greenland ice stream by 600 km and three marine-terminating glaciers connect the NEGIS with the  
44 ocean. The largest of these glaciers is Nioghalvfjærdssjøen, often named 79°N after its latitudinal  
45 position. Until recently, very few studies focused on 79°N glacier and NEGIS as they were thought to  
46 contribute little to surface mass loss and instabilities (Khan et al., 2014; Mayer et al., 2018). However,  
47 79°N glacier, with its 80 km long by 20 km wide floating tongue, has retreated by 2-3 km between  
48 2009 and 2012, and the surface of the tongue and part of the grounded section of the glacier are now  
49 thinning at a rate of 1 m yr<sup>-1</sup> (Khan et al., 2014, Mayer et al. 2018). The glacier is at a crucial  
50 interface between a warming ocean and a changing atmosphere. The mass loss from the floating  
51 tongue is largely attributed to basal melting due to the presence of warm (1°C) ocean water in the  
52 cavity below the glacier (Wilson & Straneo, 2015, Schaffer et al., 2017, Münchow et al., 2020).  
53 However, even the grounded part of the glacier is characterised by large melt ponds and drainage  
54 systems (Hochreuther, P. pers. comm); suggesting that atmospheric processes may also be at play.  
55 Furthermore, atmospheric processes may be responsible for driving the warm Atlantic water under the  
56 glacier tongue, which leads to melting of the glacier base (Münchow et al., 2020). 79°N glacier is of  
57 further interest because its southerly neighbour, Zachariae Istrom, recently lost its floating tongue  
58 (Mouginot et al., 2015).

59           A number of studies have used atmospheric modelling as a tool to investigate the region,  
60 although they have largely been confined to short case studies (Turton et al., 2019a), focused on past  
61 climates (e.g 45000 years ago by Larsen et al., 2018), or targeted specific atmospheric processes  
62 (Leeson, et al., 2018; Turton et al., 2019a). There are a number of atmospheric models that have  
63 been applied to the Greenland region, however these are often run at a resolution that is too coarse to  
64 resolve the 79°N glacier, especially its floating tongue, which can therefore be missing in many  
65 simulations. These data are usually statistically downscaled to calculate the surface mass balance of the  
66 glacier, using a digital elevation model and a shape file of the glacier. The resolution of the  
67 atmospheric models used in published studies for Greenland generally exceed 10km: e.g the Modèle  
68 Atmosphérique Régional (MAR) at 20-km (Fettweis et al, 2017) RACMO2 at 11-km (Noël et al.,  
69 2016) and HIRHAM5 at 25-km (Mottram et al., 2017a). Recently, there have been attempts at  
70 modelling the polar regions using non-hydrostatic regional climate models, including HARMONIE-  
71 AROME at 2 km resolution for the Southwest of Greenland (Mottram et al., 2017b), and the NHM-  
72 SMAP at 5 km resolution for the whole of Greenland (Niwano et al., 2018). However, the Mottram et

73 al. (2017b) study does not include the northeast of Greenland. Furthermore, the focus of the Niwano  
74 et al. (2018) study was to improve the surface mass balance estimates, as opposed to providing output  
75 for a more general atmospheric sense, and the model was not convection permitting. In convection-  
76 permitting models, typically for spatial resolutions higher than 5km, convection begins to be  
77 explicitly resolved. This can enhance the representation of convection and associated precipitation, as  
78 opposed to using a convection parameterisation scheme, (Pal et al., 2019). As yet, there are no very  
79 high-resolution, multi-year atmospheric datasets available for the northeast of Greenland or the wider  
80 region.

81 Here, we address this data gap by presenting a 5-year (2014-2018), high-resolution (1 km)  
82 atmospheric simulation using a polar-optimised atmospheric model and evaluate its skill in  
83 representing local meteorological conditions over the 79°N region in northeast Greenland. The dataset  
84 is named NEGIS\_WRF after its location of focus and model used. As the 79°N region is of growing  
85 interest, this data could be beneficial for numerous other studies and applications. Indeed, current  
86 ongoing research as part of the Greenland Ice sheet-Ocean interaction (GROCE) project  
87 ([www.groce.de](http://www.groce.de), last accessed October 1 2019) include using this data for surface mass balance studies  
88 and to investigate the relationship between specific atmospheric processes and surface melt patterns.  
89 For studies of the surface mass balance of the NEGIS, further downscaling would not be necessary.  
90 With a horizontal resolution of less than 5km, many atmospheric processes are accurately resolved  
91 including katabatic winds and warm-air advection (Turton et al., 2019a). Furthermore, high-resolution  
92 output is crucial for the complex topography on the northeast coast, where steep and variable  
93 topography can channel or block the winds, and lead to strong variability of the radiation budget. The  
94 WRF dataset is also intended as input to an ocean model, used in an ocean-glacier interaction study,  
95 input into a hydrologic model and for an ice sheet modelling study. Here we present an evaluation of  
96 the ability of NEGIS\_WRF at representing key near-surface meteorological and radiative conditions,  
97 to demonstrate the applicability of the dataset for these and other studies in the atmospheric,  
98 cryospheric and oceanic fields.

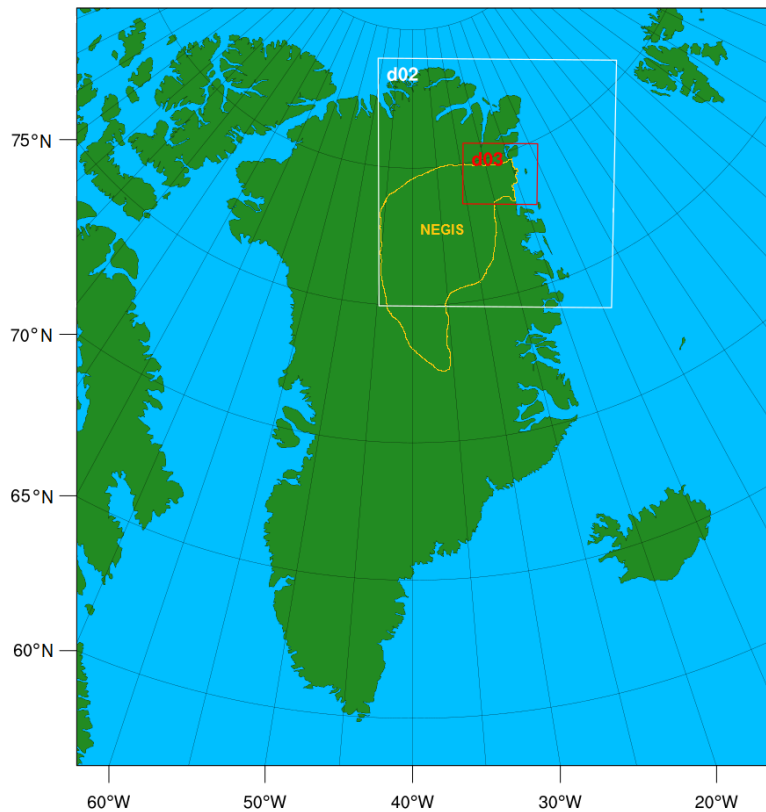
99

## 100 **2. Data and Methods**

### 101 **2.1 Model Configuration**

102 The Polar Weather Research and Forecasting (Polar WRF) model is a version of the WRF  
103 model that was developed and optimised for use in polar climates (Hines et al., 2011). The non-  
104 hydrostatic WRF model (available online from <http://www.mmm.ucar.edu/weather-research-and-forecasting-model>;  
105 last accessed July 29 2019) has been widely used for both operational studies  
106 and for research in many regions, and at many scales (Powers et al., 2017; Skamarock & Klemp,  
107 2008). The current version of polar WRF used here is v3.9.1.1, which was released in January 2018,  
108 and is available from <http://polarmet.osu.edu/PWRF/> (last accessed July 29 2019). Polar WRF has  
109 been developed for use in the Arctic and Antarctic by largely optimising the Noah Land Surface Model

110 (LSM) (Chen & Dudhia, 2001) to improve heat transfer processes through snow and permanent ice,  
111 and by providing additional methods for sea-ice treatment (Hines et al, 2015). For a full description of  
112 the Polar WRF additions, see (Hines & Bromwich, 2008; Hines et al., 2011; Hines et al., 2015) and  
113 citations therein.



114  
115 **Figure 1: The domain configuration for the Polar WRF runs and the approximate outline of**  
116 **NEGIS following Khan et al. (2014).**

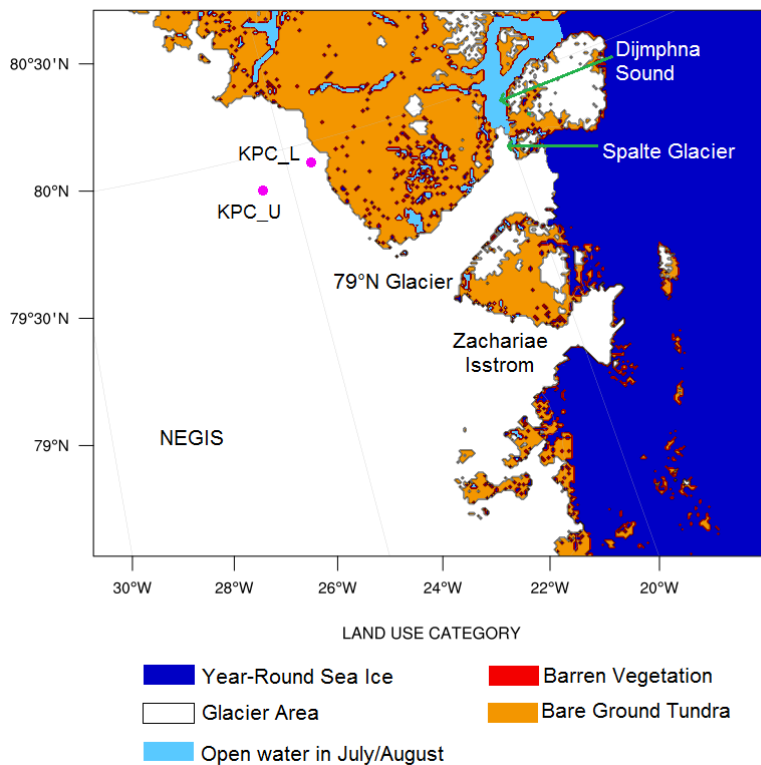
117  
118 The meteorological initialisation and boundary input data is from the ECMWF (European  
119 Centre for Medium range Weather Forecast) ERA-Interim dataset at 6-hourly intervals (Dee et al.,  
120 2011). This reanalysis product was more accurate at resolving mesoscale processes in the northeast of  
121 Greenland compared to MERRA2 reanalysis data and has previously been used for Polar WRF  
122 simulations in Greenland (DuVivier & Cassano, 2013; Turton et al., 2019a). The Sea Surface  
123 Temperature (SST) and sea ice concentration values are from the NOAA Optimum Interpolation  
124 0.25° resolution daily data. This is a combination of data from the Advanced Very High Resolution  
125 Radiometer (AVHRR) infrared satellite and Advanced Microwave Scanning Radiometer (AMSR)  
126 (doi:10.5065/EMOT-1D34, data retrieved from <https://rda.ucar.edu/datasets/ds277.7/>, last accessed  
127 July 29 2019). In-situ ship and buoy data are used to correct satellite biases, leading to relatively low  
128 mean biases of 0.2-0.4K for SST data (more information on this dataset can be found in Banzon et al.,  
129 2016). This higher resolution dataset was required due to the very blocky coastline in the SST and sea

130 ice data from ERA-Interim. The domain setup is shown in Figure 1. The outermost domain (D01) is at  
131 25km, D02 is 5km and D03 (innermost) is 1km grid spacing. Boundary conditions, including sea ice  
132 fraction and SST were updated every 6-hours. Analysis nudging was used in the outer domain (D01)  
133 to constrain the large-scale circulation while allowing the model to freely simulate in D02 and D03.  
134 Nudging is the process of constraining the interior of model domains towards the larger-scale field  
135 (from reanalysis data) which drive the simulation (Lo et al., 2008., Otte et al., 2012). It has been  
136 found to improve simulations of the large-scale circulation (Bowden et al., 2012) and reduce errors in  
137 the mean and extreme values (Otte et al., 2012) from relatively long runs. We only nudge the outer  
138 domain (D01) to allow the higher-resolution domain to evolve freely. The USGS 24 category landuse  
139 and landmask was adjusted using the European Space Agency (ESA) Climate Change Initiative (CCI)  
140 landuse product, to provide a better representation of the glacier outlines and the terminus of the  
141 floating tongue (<https://www.esa-landcover-cci.org/>, last accessed September 5 2019). A number of  
142 open-water grid points were manually changed to glacierised during January-June and September-  
143 December to better represent the floating tongue of the Spalte Glacier (tributary of 79°N on the  
144 northeast side) and the sea ice in the adjacent Dijnphna Sound (Fig. 2). Other small exposed water  
145 areas along the coast, which are permanently frozen except in July and August each year  
146 (Hochreuther, P., 2019 personal communication), were also changed to ice during all months except  
147 July and August (Fig. 2). The glacier extents are treated as static throughout the run, which is an  
148 appropriate approximation given the small and likely negligible area of calving of 79°N during our  
149 study period (see ENVEO, 2019 for calving front locations from 1990 to 2017). There are 60 levels in  
150 the vertical, with a 10-hPa model top and a lowest model level ~16m above the surface.

151 Many of the parameterisations for the model configuration were selected based on numerous,  
152 previous Polar WRF runs over Greenland and the Arctic (for example Hines et al., 2011). In brief, the  
153 following parameterisations were employed: the Noah LSM (Chen & Dudhia, 2011), due to its  
154 optimisations that have been tested over Greenland (Hines & Bromwich, 2008), Arctic sea ice (Hines,  
155 et al 2015) and Arctic land (Hines et al., 2011); the Morrison two-moment scheme for microphysics,  
156 which has been shown to out-perform other schemes in both Polar regions (Bromwich, et al., 2009;  
157 Lachlan-Cope, et al., 2016; Listowski & Lachlan-Cope, 2017); the Eta Similarity Scheme for surface  
158 layer physics (Janjić, 1994) and the Yonsei University Scheme for planetary boundary layer  
159 parameterisation. This was used due to the topographic wind scheme (Hong et al., 2006) that can  
160 correct excessive wind speeds in areas of complex topography, such as the northeast coast of  
161 Greenland (employed in D02 and D03 only, where complex orography is best resolved). Further  
162 parameterisations include: the Kain-Fritsch scheme for cumulus convection (Kain, 2004) (D01 and  
163 D02 only, as the resolution of D03 allows convection to be explicitly resolved); and, the Rapid  
164 Radiative Transfer Model (RRTM) longwave and Goddard shortwave schemes for radiation, based  
165 on sensitivity testing for the polar regions by Hines et al. (2008) and subsequent runs over Greenland  
166 (DuVivier & Cassano, 2013; Hines et al., 2011). Whilst the majority of these options were selected

167 for testing based on the works of other publications, a short sensitivity study was also conducted,  
 168 alongside with testing the horizontal and vertical resolution and locations of the domains (not  
 169 included). It was found that a combination of the options above were best suited to the northeast of  
 170 Greenland when compared with observations on the floating tongue of the 79°N glacier from 1996-  
 171 1999 (Turton et al., 2019a).

172 Other options specified for this study include using a fractional sea ice treatment, which  
 173 allows calculation of different surface temperature, surface roughness and turbulent fluxes for open  
 174 water and sea ice conditions within the grid cell, and then calculates an area-weighted average for the  
 175 grid (DuVivier & Cassano, 2013; Hines et al., 2011). The adaptive timestep was used to optimise the  
 176 simulation speed. For each year simulated, the model was initialised on September 1 before the onset of  
 177 the accumulation season and ran continuously until October 1 of the following year (e.g September 1  
 178 2016 - October 1 2017). September was then discarded as a spin up month. The model produces  
 179 similar magnitude snow depths to available observations (Pedersen et al. 2016). Due to limited  
 180 snowfall and snow depth observations in this region, we compared cumulative snowfall to ERA5  
 181 products during testing, which have been shown to have a relatively good agreement with  
 182 observations by Wang et al. (2019). The maximum snow depth and average annual accumulation  
 183 were well captured by Polar WRF compared to ERA5.



184  
 185 **Figure 2: A map of the land use types for D03. Colours represent the land use type, except for**  
 186 **light blue, which highlights the manually changed land use from open water to sea ice during**

187 **winter. Important locations are also highlighted, as are the locations of the two AWS sites (pink**  
188 **dots).**

189

190 The data were output at hourly intervals for D03, at six-hourly intervals for D02 and at daily intervals  
191 for D01. Daily mean values for key meteorological variables from D02 and D03 were calculated from  
192 the hourly values and are available along with the daily instantaneous values from D01 at the Open  
193 Science Framework repository (Turton et al. 2019b: doi.org/10.17605/OSF.IO/53E6Z).

194

## 195 **2.2 Observational Data**

196 The remote nature of the location of interest provides few in-situ observational datasets for model  
197 evaluation. However, the PROMICE (Programme for Monitoring of the Greenland Ice Sheet) network  
198 (www.promice.dk, last accessed October 1 2019; van As & Fausto, 2011), operated by the Geological  
199 Survey of Denmark and Greenland (GEUS) has two permanent Automatic Weather Stations (AWSs)  
200 available for comparison of daily means of meteorological variables and a number of surface energy  
201 balance components. The AWSs are referred to as KPC\_L and KPC\_U due to their location on  
202 Kronprins Christian Land (located to the northwest of 79°N glacier; see Table 1 for AWS details of  
203 location, dates and available variables. Although hourly data are available, daily means are used for  
204 evaluation due to the multi-year timescale of the study, but the authors note that an evaluation of  
205 hourly data should be performed before using these data for analysis at these time scales. Please refer  
206 to van As & Fausto, (2011) and Turton et al., (2019a) for more information on the PROMICE data in  
207 this location (doi.org/10.22008/promice/data/aws, available at [www.promice.dk](http://www.promice.dk), last accessed  
208 October 1 2019). Observations are not taken at exactly 2m above the surface but vary with  
209 accumulation and ablation. Over bare ice, the sensor is 2.6m above the surface (van As et al., 2011).  
210 To clarify that the observations represent near-surface conditions, and are compared with 2m and 10m  
211 model output, we use the abbreviation X2 or X10 to represent both modelled and observed variables  
212 at the respective heights. The mean values from the observational data are calculated from daily  
213 averages from January 1 2014- December 31 2018 to keep a consistent period across all data.

214 The in-situ AWS observational data are used to evaluate the NEGIS\_WRF output and to  
215 provide a judgement of its skill to benefit future users. The focus of the evaluation is to test WRF's  
216 ability to represent local meteorological conditions over a polar glacier. Daily mean values from  
217 NEGIS\_WRF have been calculated from hourly output at the location of the two AWSs. All  
218 evaluation focuses on near-surface meteorological output from D03.

219

220 **Table 1: The location, elevation and data availability of the two AWSs used for model**  
221 **evaluation. We evaluate the model output with four variables from the AWSs. Data was**  
222 **unavailable at KPC\_L between January 15 2010 and July 17 2012 due to retrieval problems. T**  
223 **is air temperature, Q is specific humidity, WS and WD are wind speed and direction,**

224 respectively. Observations are taken at approximately 2m above the surface, but this does vary  
 225 with accumulation and ablation (see section 2.2). Sensor error estimates come from the sensor  
 226 manufacturers. See van As & Fausto (2011) for more information on sensors and observations.

Name	Location	Elevation (m a.s.l)	Data Availability	Variables used for evaluation	Sensor Error Estimates
KPC_L	79.91°N, 24.08°W	380	01.01.2009- present	T, Q, WS, WD, SW <sub>down</sub> , LW <sub>down</sub>	T: ± 0.2°C RH: ± 1.5% WS: ± 0.3ms <sup>-1</sup> WD: ± 3° Radiation: 10%
KPC_U	79.83°N, 25.17°W	870	01.01.2009- 14.01.2010,  18.07.2012-present	T, Q, WS, WD, SW <sub>down</sub> , LW <sub>down</sub>	T: ± 0.2°C RH: ± 1.5% WS: ± 0.3ms <sup>-1</sup> WD: ± 3° Radiation: 10%

227

### 228 3. Results

#### 229 3.1 Model evaluation: Daily Means

230 The air temperature is simulated well by the WRF simulations with a coefficient of determination ( $R^2$ )  
 231 of 0.92 at both KPC\_L and KPC\_U (Table 2, Fig 3). Similarly, the mean biases and RMSE are small.  
 232 The mean bias and RMSE are slightly larger during winter (DJF) at KPC\_U, but overall, the  $R^2$  value  
 233 at both locations remains above 0.64. The particularly low daily temperatures observed during winter  
 234 at KPC\_U are not fully captured by the WRF simulations (Fig. 3b). The model can, however, capture  
 235 the larger variability in winter (Fig. 3), including ‘warm-air events’, where the air temperature  
 236 increases by more than 10°C in a few days, leading to temperatures above the average for winter  
 237 (Turton et al., 2019a). Figure 4 presents the near-surface air temperature and 10m wind vectors for  
 238 June 6 2015, to show what the temperature and wind fields look like for an example time period  
 239 during the ablation period (June to August). The onset of the ablation season is earlier over the  
 240 floating tongue of the glacier, as seen by the above freezing air temperatures at low elevations in  
 241 Figure 4. WRF simulates the humidity very well annually and during winter for both locations. The  
 242 humidity during summer is slightly less well simulated, with mean biases of 0.4 and 0.6 g/kg for  
 243 KPC\_L and KPC\_U respectively (Table 2). However, the  $R^2$  values remain above 0.44 for the  
 244 summer season. For both locations, annually and seasonally, WRF is moister than in observations,  
 245 however the mean biases remain relatively small (less than 0.6 g/kg), and the differences are not



246 statistically significant except for during summer at KPC\_U (which is statistically different at the 99%  
 247 confidence level using a student t-test). The wind direction in WRF deviates more from the AWS data  
 248 than for temperature and moisture, which is likely due to the particularly steep and complex  
 249 topography of the region which may not be accurately represented by the model, even at 1 km  
 250 resolution. The largest bias is an annual bias at KPC\_L (10.7°) as WRF simulates the wind direction  
 251 predominantly more northerly than in observations (Table 2), which leads to poor  $R^2$  values (0.01) and  
 252 high RMSE. For KPC\_U annually and seasonally, the biases remain at or below 8.6° and  $R^2$  values  
 253 are 0.36, which shows that WRF is capable of representing the wind direction at KPC\_U. Some of  
 254 these errors may relate to measurement errors of the wind sensor, which is  $\pm 3^\circ$  (see Table 1). The  
 255 model performs better at simulating the wind speed than the wind direction. Annually and during  
 256 winter, the  $R^2$  values are relatively high (above 0.31) at both locations, and mean biases remain at or  
 257 below  $2.3 \text{ ms}^{-1}$  both annually and seasonally. None of the biases between WRF and observations are  
 258 statistically significantly different for daily mean wind speed or air temperature (Table 2).

259 Shortwave and longwave radiation values are important for a range of possible future studies  
 260 including input to surface mass balance and ocean models. Therefore, we have validated the  
 261 NEGIS\_WRF output for both the downwelling shortwave and longwave by comparing it to  
 262 observations at the two sites (Table 2). Annually, the biases are within sensor error range (Table 1)  
 263 and differences between WRF and observations are not statistically significant for both downwelling  
 264 shortwave ( $SW_{\text{down}}$ ) and longwave ( $LW_{\text{down}}$ ). Due to the lack of sunlight during winter at this latitude,  
 265 the  $SW_{\text{down}}$  biases and RMSE are small and the  $R^2$  values (0.78 and 0.75 for KPC\_L and KPC\_U  
 266 respectively) are high for both locations (Table 2). The mean biases are largest for  $SW_{\text{down}}$  during  
 267 summer, but a relatively high  $R^2$  value shows that WRF still has a great deal of skill (0.82 at KPC\_U).  
 268 Biases for  $LW_{\text{down}}$  are largest during winter (-10.3 and -15.3  $\text{Wm}^{-2}$  at KPC\_L and KPC\_U  
 269 respectively), which is likely a product of increased wintertime variability due to storm frequency and  
 270 location (van As et al., 2009). Similarly, Cho et al. (2020) found that biases of  $LW_{\text{down}}$  compared to  
 271 satellite observations were larger for the Morrison microphysics scheme (which we use here) than for  
 272 the WRF single moment 6-class scheme. However, it was concluded that Polar WRF has the ability to  
 273 accurately simulate the spatial distribution of Arctic clouds and their optical properties with both  
 274 tested schemes (Cho et al., 2020). None of the differences between WRF output and observations for  
 275 the radiation components were statistically significant (Table 2).

276

277 **Table 2: Comparison of the near-surface WRF model output to AWS data at KPC\_L and**  
 278 **KPC\_U. ANN refers to annual mean values, DJF refers to winter average values whereas JJA**  
 279 **refers to summer average values. \* refers to statistically significant differences between WRF**  
 280 **and AWS at the 99% confidence interval, using the student's t-test.**

Variable (units)	Location	AWS Mean	Mean Bias	RMSE	$R^2$
------------------	----------	----------	-----------	------	-------

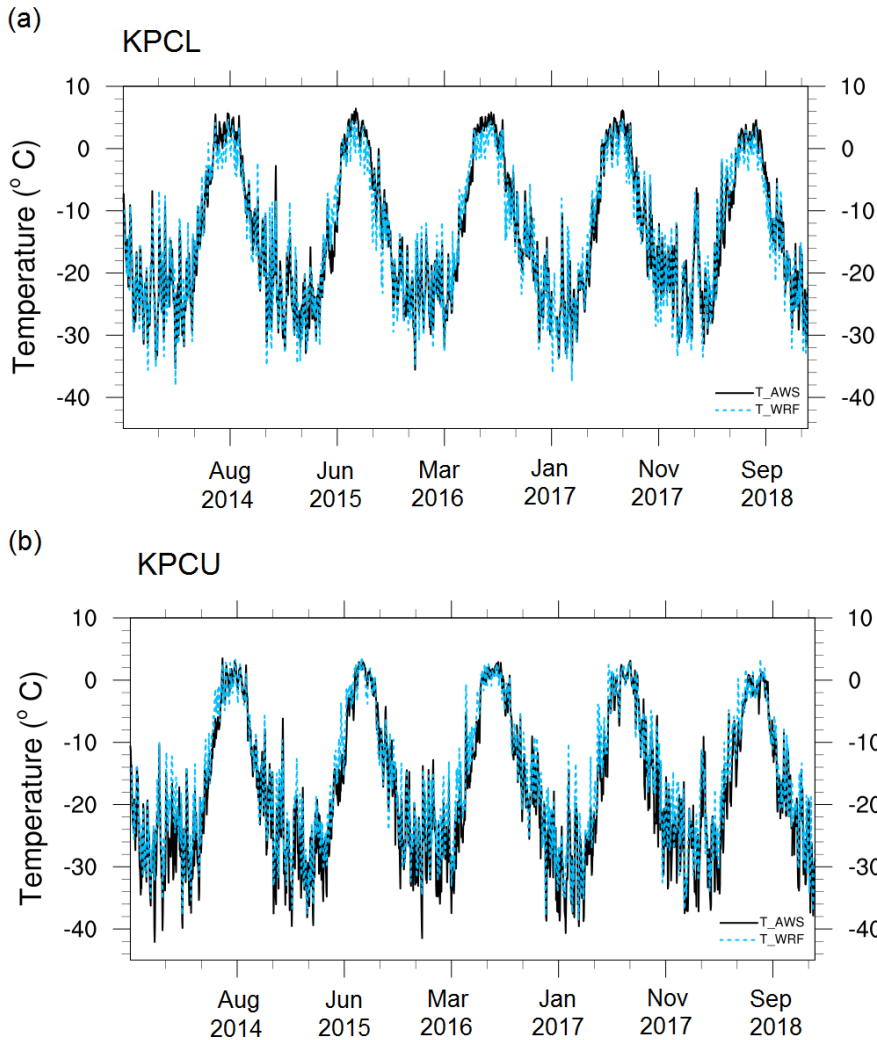
			(WRF-AWS)		
<b>T2 ANN (°C)</b>	<b>KPC_L</b>	<b>-13.6</b>	<b>-0.3</b>	<b>3.0</b>	<b>0.92</b>
	<b>KPC_U</b>	<b>-17.2</b>	<b>1.8</b>	<b>4.0</b>	<b>0.92</b>
<b>T2 DJF (°C)</b>	<b>KPC_L</b>	<b>-23.3</b>	<b>0.0</b>	<b>3.2</b>	<b>0.86</b>
	<b>KPC_U</b>	<b>-27.6</b>	<b>2.6</b>	<b>5.2</b>	<b>0.64</b>
<b>T2 JJA (°C)</b>	<b>KPC_L</b>	<b>1.6</b>	<b>-1.8</b>	<b>2.6</b>	<b>0.71</b>
	<b>KPC_U</b>	<b>-1.5</b>	<b>-0.1</b>	<b>1.9</b>	<b>0.69</b>
<b>Q2 ANN (g/kg)</b>	<b>KPC_L</b>	<b>1.6</b>	<b>0.2</b>	<b>0.4</b>	<b>0.92</b>
	<b>KPC_U</b>	<b>1.4</b>	<b>0.3</b>	<b>0.5</b>	<b>0.92</b>
<b>Q2 DJF (g/kg)</b>	<b>KPC_L</b>	<b>0.4</b>	<b>0.1</b>	<b>0.1</b>	<b>0.81</b>
	<b>KPC_U</b>	<b>0.3</b>	<b>0.1</b>	<b>0.2</b>	<b>0.66</b>
<b>Q2 JJA (g/kg)</b>	<b>KPC_L</b>	<b>3.2</b>	<b>0.4</b>	<b>0.8</b>	<b>0.44</b>
	<b>KPC_U</b>	<b>3.0</b>	<b>0.6*</b>	<b>0.9</b>	<b>0.56</b>
<b>WD10 ANN (°)</b>	<b>KPC_L</b>	<b>219.4</b>	<b>10.7*</b>	<b>74.3</b>	<b>0.01</b>
	<b>KPC_U</b>	<b>277.9</b>	<b>3.4</b>	<b>29.9</b>	<b>0.36</b>
<b>WD10 DJF (°)</b>	<b>KPC_L</b>	<b>238.5</b>	<b>-3.2</b>	<b>49.9</b>	<b>0.01</b>
	<b>KPC_U</b>	<b>274</b>	<b>8.6</b>	<b>29.1</b>	<b>0.36</b>
<b>WD10 JJA (°)</b>	<b>KPC_L</b>	<b>211.6</b>	<b>6.8*</b>	<b>80.2</b>	<b>0.01</b>
	<b>KPC_U</b>	<b>279.9</b>	<b>-0.1</b>	<b>31.7</b>	<b>0.25</b>
<b>WS10 ANN (m/s)</b>	<b>KPC_L</b>	<b>5.7</b>	<b>0.4</b>	<b>2.9</b>	<b>0.42</b>
	<b>KPC'_U</b>	<b>4.8</b>	<b>1.5</b>	<b>2.5</b>	<b>0.49</b>
<b>WS10 DJF (m/s)</b>	<b>KPC_L</b>	<b>6.4</b>	<b>1.0</b>	<b>3.2</b>	<b>0.50</b>
	<b>KPC_U</b>	<b>5.2</b>	<b>2.3</b>	<b>3.4</b>	<b>0.38</b>
<b>WS10 JJA (m/s)</b>	<b>KPC_L</b>	<b>5.4</b>	<b>-0.8</b>	<b>2.7</b>	<b>0.31</b>
	<b>KPC_U</b>	<b>4.2</b>	<b>0.8</b>	<b>1.9</b>	<b>0.45</b>
<b>SW<sub>down</sub> ANN (Wm<sup>-2</sup>)</b>	<b>KPC_L</b>	<b>114.5</b>	<b>4.7</b>	<b>34.1</b>	<b>0.94</b>
	<b>KPC_U</b>	<b>124.6</b>	<b>3.8</b>	<b>23.8</b>	<b>0.97</b>
<b>SW<sub>down</sub> DJF (Wm<sup>-2</sup>)</b>	<b>KPC_L</b>	<b>0.1</b>	<b>-0.1</b>	<b>0.4</b>	<b>0.78</b>
	<b>KPC_U</b>	<b>0.2</b>	<b>-0.1</b>	<b>0.5</b>	<b>0.75</b>
<b>SW<sub>down</sub> JJA (Wm<sup>-2</sup>)</b>	<b>KPC_L</b>	<b>271.6</b>	<b>13.1</b>	<b>62.3</b>	<b>0.63</b>
	<b>KPC_U</b>	<b>295.1</b>	<b>11.9</b>	<b>42.2</b>	<b>0.82</b>
<b>LW<sub>down</sub> ANN (Wm<sup>-2</sup>)</b>	<b>KPC_L</b>	<b>212.0</b>	<b>-7.1</b>	<b>24.7</b>	<b>0.76</b>
	<b>KPC_U</b>	<b>202.5</b>	<b>-9.2</b>	<b>26.1</b>	<b>0.71</b>
<b>LW<sub>down</sub> DJF (Wm<sup>-2</sup>)</b>	<b>KPC_L</b>	<b>181.9</b>	<b>-10.3</b>	<b>26.8</b>	<b>0.50</b>
	<b>KPC_U</b>	<b>179.6</b>	<b>-15.3</b>	<b>31.6</b>	<b>0.40</b>

<b>LW<sub>down</sub> JJA (Wm<sup>-2</sup>)</b>	<b>KPC_L</b>	<b>267.3</b>	<b>-4.9</b>	<b>23.8</b>	<b>0.38</b>
	<b>KPC_U</b>	<b>250.8</b>	<b>-6.4</b>	<b>21-6</b>	<b>0.49</b>

281

282 The larger RMSE and lower R<sup>2</sup> values during summer for wind direction can, at least partly, be  
283 attributed to the larger variability of those variables during summer. In summer (JJA), the average  
284 deviation of wind direction in observations at KPC\_L is 40.3°. Whilst WRF is able to capture this  
285 variability in wind direction (the average deviation is 41.1°), there is sometimes an offset in the timing  
286 of the wind direction change between WRF and observations. For example, after two weeks of  
287 consistently northwesterly winds being observed at KPC\_L between August 11 to 24, 2014, there was  
288 a shift to northeasterly flow on the morning of August 25 2014 (Fig 5e). WRF successfully simulated  
289 the long period of northwesterly winds, and the shift to winds from the northeast, however the change  
290 in direction was simulated in the late evening of August 25 to early morning of August 26 (Fig. 5f),  
291 leading to a bias of 156.9° on August 25. The northeasterly wind was only observed for 24 hours  
292 before returning to westerly on August 26 (Fig. 5g). WRF was able to capture the short-lived timing  
293 of the event, but 24 hours later. In this particular case, the wind direction error comes from the  
294 boundary data, ERA-Interim. In ERA-Interim, the wind direction change starts on August 24 but  
295 remains northerly until 18:00 UTC on August 25. It then remains northeasterly until August 27, which  
296 is 24-hours longer than in near-surface observations. The later onset and more persistent flow from the  
297 northeast in ERA-Interim likely led to the later onset of northeasterly flow in WRF. Therefore, WRF  
298 can capture both the predominant wind flow, and abrupt changes to the wind direction, along with  
299 capturing even short-lived events, although the timing is occasionally shifted. Figure 5 also highlights  
300 that whilst the annual mean bias for wind speed is less than 1.5 ms<sup>-1</sup> (Table 2), during certain periods,  
301 WRF simulates higher wind speeds than observed. However, these are not unrealistic values for this  
302 region, with a maximum observed wind speed of 20.2 ms<sup>-1</sup> and a maximum simulated wind speed of  
303 22.3 ms<sup>-1</sup> for the KPCL location. The largest values and biases of wind speed occur during  
304 particularly strong katabatic events (northwesterly wind direction during winter). This was also found  
305 by Hines & Bromwich (2008) when using the same land surface scheme as in these simulations.

306 Overall, WRF performs well at simulating air temperature, humidity, downwelling radiation  
307 and wind speed during the simulation period (Oct 2013 - Dec 2018). WRF struggles to as accurately  
308 represent the wind direction, especially at KPC\_L (which is likely due to the proximity of complex  
309 topography to the KPC\_L site), however the winds remain predominantly westerly to northwesterly,  
310 which shows that WRF can capture the dominant katabatic process governing the wind directions.



311  
 312 **Figure 3: The observed (black lines) and modelled (dashed blue lines) daily average air**  
 313 **temperature at KPC\_L (top) and KPC\_U (bottom) from D03.**

314  
 315 **3.2 Model evaluation: Sub-daily Data**

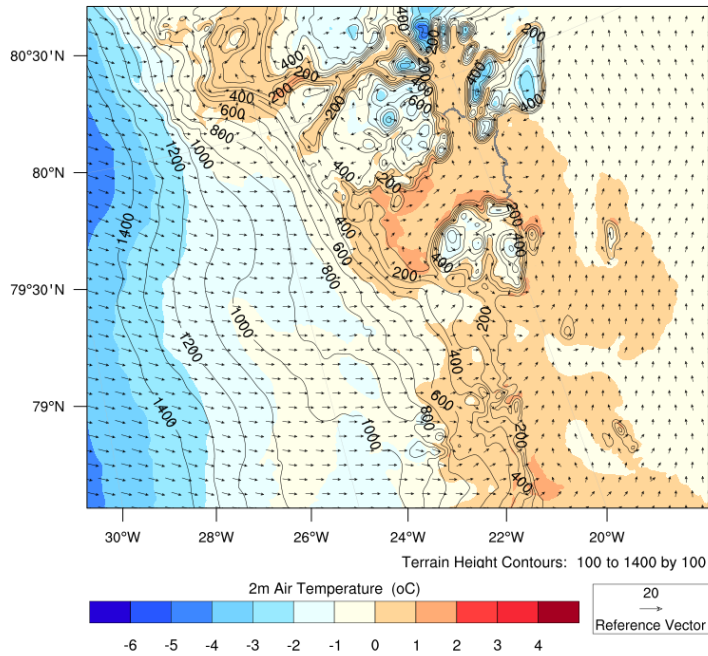
316 To evaluate the ability of the model to simulate sub-daily values, the minimum and maximum daily  
 317 near-surface values (from hourly output) are compared to observations, and the amplitude of the  
 318 diurnal cycle of air temperature is also evaluated. Figure 6 presents the statistics for daily minimum  
 319 and maximum air temperatures at the two locations in observations and WRF. The median values are  
 320 well captured by WRF, especially for the maximum daily values, where a median value of  $-13.9^{\circ}\text{C}$  is  
 321 observed at KPC\_U, and  $-14.0^{\circ}\text{C}$  is simulated. Similarly, for maximum temperatures, the 75<sup>th</sup> quartile  
 322 values are well captured by WRF (Fig. 6). For KPC\_L, the minimum and maximum temperatures are  
 323 colder in WRF than in observations. For example, the 25<sup>th</sup> percentile value for the minimum  
 324 temperatures (far left bar in Fig. 6) is  $3.8^{\circ}\text{C}$  in observations, but  $6.3^{\circ}\text{C}$  in WRF. At KPC\_U, the

325 opposite is true, where WRF simulates slightly higher temperatures than in observations. However,  
326 overall, the range of minimum and maximum temperature values are well modelled by WRF.

327 The average daily maximum air temperature observed at KPC\_L is  $-21.0^{\circ}\text{C}$  in winter (DJF)  
328 and increases to  $3.0^{\circ}\text{C}$  in summer (JJA). WRF simulates an average daily maximum of  $-20.9^{\circ}\text{C}$  in  
329 winter, which increases to  $0.9^{\circ}\text{C}$  in summer. The average daily minimum air temperature observed at  
330 KPC\_L is  $-25.9^{\circ}\text{C}$  during winter and rises to  $0.2^{\circ}\text{C}$  in summer. WRF simulates an average daily  
331 minimum air temperature of  $-26.5^{\circ}\text{C}$  in winter and increasing to  $-2.3^{\circ}\text{C}$  in summer. Therefore, WRF is  
332 able to accurately simulate the winter minimum and maximum temperatures. WRF slightly  
333 underestimates the air temperature during summer, however at KPC\_U, this is within the error  
334 estimate provided by the sensor manufacturer (Table 1), and for both locations the biases are not  
335 statistically significant (Table 2).

336 Similarly, at KPC\_U, the observed maximum temperature values are  $-24.1^{\circ}\text{C}$  in winter and  
337  $0.1^{\circ}\text{C}$  in summer. From WRF, the average maximum temperature is  $-22.5^{\circ}\text{C}$  in winter and increases  
338 to  $-0.1^{\circ}\text{C}$  in summer. The observed minimum daily air temperature at KPC\_U is  $-30.8^{\circ}\text{C}$  during  
339 winter and  $-3.5^{\circ}\text{C}$  in summer. In comparison, in the WRF simulations, the average daily minimum  
340 temperature is  $-27.4^{\circ}\text{C}$  during winter and increases to  $-3.9^{\circ}\text{C}$  in summer. WRF can therefore represent  
341 the maximum and minimum daily air temperatures at KPC\_U.

342 The annual-average observed diurnal air temperature amplitude is  $5.6^{\circ}\text{C}$  at KPC\_U and  $4.0^{\circ}\text{C}$   
343 at KPC\_L. The largest average diurnal cycle is observed during spring (MAM) at KPC\_U ( $6.8^{\circ}\text{C}$ ) and  
344 during winter at KPC\_L ( $4.9^{\circ}\text{C}$ ). The WRF model simulated an average diurnal amplitude of  $5.0^{\circ}\text{C}$  at  
345 KPC\_U  $4.7^{\circ}\text{C}$  at KPC\_L. The largest diurnal cycles are simulated during spring at KPC\_U ( $6.2^{\circ}\text{C}$ )  
346 and during winter at KPC\_L ( $5.5^{\circ}\text{C}$ ). Therefore, WRF accurately simulates the timing of the largest  
347 diurnal amplitudes but overestimates the amplitude slightly at KPC\_L, and underestimates it at  
348 KPC\_U, both by  $0.6^{\circ}\text{C}$ . The relatively large diurnal amplitude in winter may be counterintuitive given  
349 that the glacier is located in the Arctic, where polar night (no solar radiation) prevails throughout  
350 winter. However, the temperature variability is largest during winter over the glacier due to the more  
351 frequent passing of storms across the Atlantic Ocean and the occurrence of ‘warm-air events’ from  
352 easterly horizontal advection and increased longwave radiation from clouds (van As et al. 2009,  
353 Turton et al. 2019a). Warm-air events are characterised by large ( $>10^{\circ}\text{C}$ ) temperature increases  
354 between November and March, which can last for a number of days and, on average, occur 10 times  
355 per year (standard deviation of 4.0) (Turton et al., 2019a). The variability can be further enhanced by  
356 turbulent mixing from katabatic winds and the presence of föhn winds (Turton et al., 2019a).



357

358 **Figure 4: The 2m air temperature (colours), wind vectors (arrows) and terrain height contours**  
 359 **(black lines) for June 6 2015. The edge of 79°N glacier is shown by the dark grey line.**

360

361

362

363

364

365

366

367

368

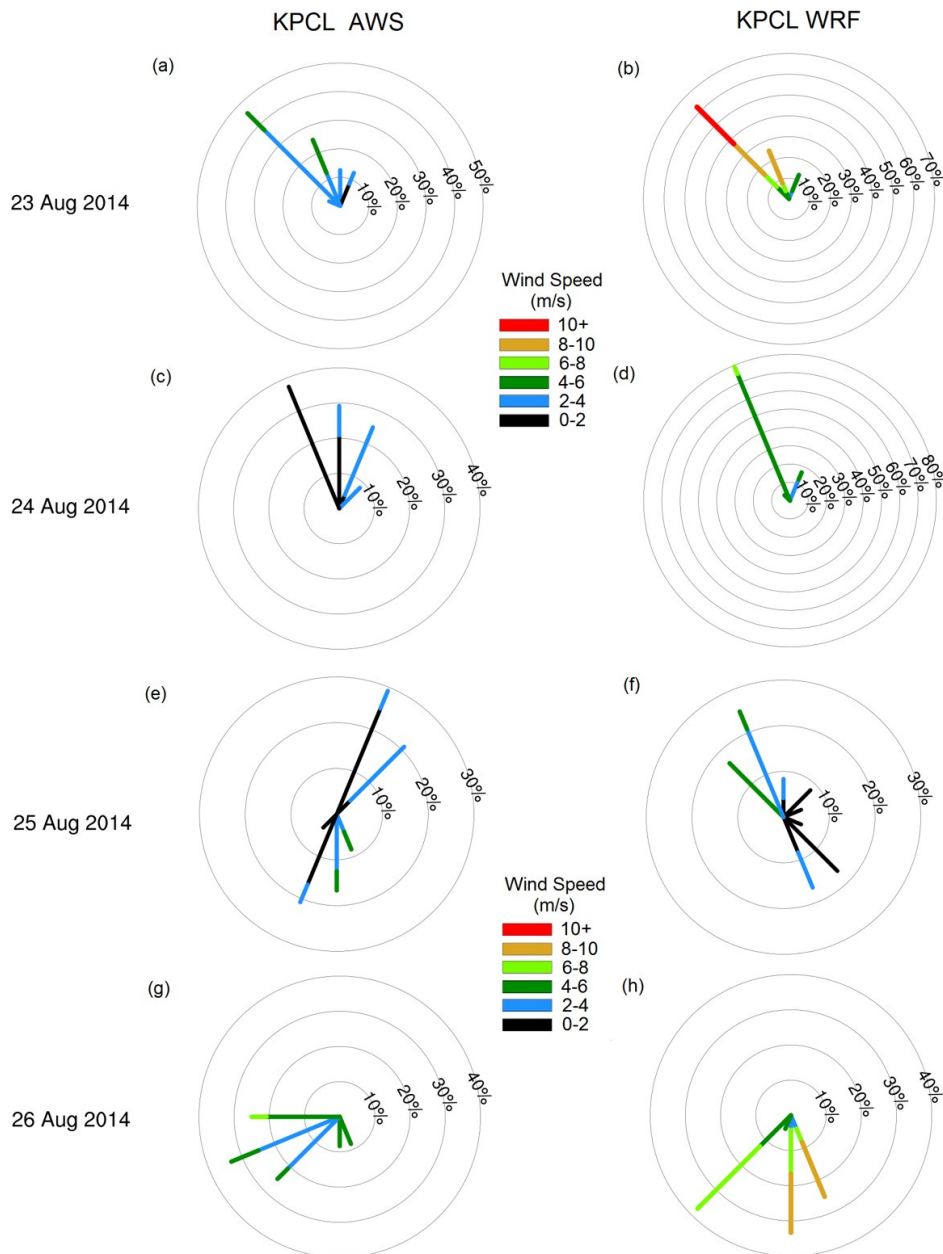
369

370

371

The maximum hourly air temperature over the four years of data observed at KPC\_L was on July 23, 2014 (8.1°C) (Fig. 6). WRF was able to replicate the processes responsible for the particularly warm day, as a daily maximum value of 4.5°C was modelled at KPC\_U. At KPC\_L, the maximum was simulated 24-hours earlier (6.5°C). The maximum values from WRF are slightly lower than observed (Fig. 6), but the timing of the maximum was accurate. The lower maximum values are likely linked to the negative mean bias in temperature simulated by WRF during the summer months (Table 2).

The absolute minimum hourly air temperature was observed at KPC\_U on December 26, 2015 (-45.0°C) (Fig. 6) and on December 27, 2015 at KPCL (-37.2°C). Again, WRF was able to capture the events leading to the particularly cold December 2015 period. On December 27, the simulated minimum air temperature was -37.7°C at KPC\_L and -37.8°C at KPC\_U. The minimum daily values are warmer than those observed at KPC\_U, but very similar to those observed at KPC\_L. (Table2).



372 **Figure 5: Wind speed (colour) and direction (lines) for August 23 to 26, 2014, from observations**  
 373 **(left panel) and WRF (right panel) at KPC\_L location. The circles (and therefore length of the**  
 374 **spikes) represent the frequency of the particular wind direction, with the percentage of**  
 375 **occurrence written on the circles.**

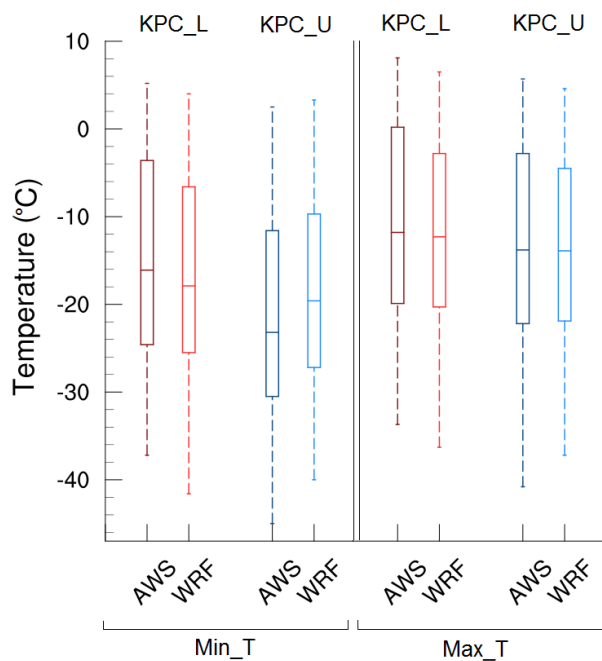
376

#### 377 **4. Conclusions**

378 Polar WRF has previously been extensively used in the Arctic (e.g Hines et al., 2011; Hines, &  
 379 Bromwich, 2017; Wilson et al., 2011), including for Greenland (e.g DuVivier & Cassano., 2013;  
 380 Turton et al., 2019a), for a number of applications. However, WRF runs have often been used for  
 381 short case studies or performed at lower spatial resolution. This dataset provides high spatial and  
 382 temporal resolution runs over multiple years (2014-2018) for an area of increased interest. Regardless

383 of the regular use of Polar WRF, it remains important to validate the model for specific locations,  
384 especially when downscaling to very high resolutions.

385 Overall, the mean biases are small and statistically insignificant between the Polar WRF runs  
386 and the PROMICE observations at both the lower and upper stations near 79°N glacier. The  $R^2$   
387 values are high for air temperature, humidity and wind speed, but less so for wind direction at  
388 KPC\_L. The wind direction is more variable in summer than in other months, and whilst WRF is able  
389 to simulate the increased variability, large biases can arise due to inconsistent timing of wind direction  
390 changes between WRF and observations over short periods of 24-hours or less. However, as WRF is  
391 able to replicate the short-lived events and the predominant northwesterly winds of katabatic origin,  
392 we can conclude that the NEGIS\_WRF can be used for further studies of the near-surface meteorology  
393 of the 79°N glacier. This dataset will be useful for many other applications in a number of fields  
394 including the atmospheric and cryospheric sciences, and as input to hydrological, ice sheet and ocean  
395 models, subject to appropriate validation.



396  
397

398 **Figure 6: Box plot representing the minimum (left) and maximum (right) daily temperature**  
399 **values at KPC\_L (red) and KPC\_U (blue) locations, from both observations (darker colours)**  
400 **and WRF (lighter colours).**

401

## 402 5. Data Availability

403 The atmospheric dataset, NEGIS\_WRF resolves for the first time, the meteorological conditions over  
404 the northeast region of Greenland (5km) and 79°N glacier region at the kilometre scale over a period  
405 of five years (2014-2018). More than 50 variables are available (near-surface and on 60 atmospheric  
406 levels) at up to hourly temporal resolution (for the 1 km domain), including meteorological and



407 radiative fields. Daily mean values for near-surface temperature (2m), specific humidity (2m), skin  
408 temperature, and U and V wind components (10m) are available online (Turton et al 2019b:  
409 [doi.org/10.17605/OSF.IO/53E6Z](https://doi.org/10.17605/OSF.IO/53E6Z)) for the 1km and 5km domains from 2014-2018. As the output  
410 frequency from D01 (25km resolution) was once per day, the available values are instantaneous daily  
411 values at 00 UTC, as opposed to daily means. Furthermore, 4-D variables of temperature, humidity, U  
412 and V wind components, geopotential and pressure are available on model levels at the same  
413 frequency as the near-surface variables. For other variables, or more frequent output, please contact  
414 the lead author, and these can be made available. Due to the large amount of data, these are not stored  
415 online, but at the Regional Computation Centre Erlangen (RRZE) in Germany.

416

## 417 **6. Author Contributions**

418 JVT wrote the paper, ran the WRF model and evaluated it against the observations. TM and EC  
419 contributed to the research concept, discussion, optimisation of the simulations and manuscript  
420 refinement.

421

## 422 **7. Competing Interests**

423 The authors have no competing interests.

424

## 425 **8. Acknowledgements**

426 We thank Dirk van As from GEUS for his assistance with the PROMICE data and to Keith Hines for  
427 the Polar WRF code. The authors also thank two anonymous reviewers and Dr Yasuhiro Murayama  
428 for improving and editing our manuscript. This work was supported by the German Federal Ministry  
429 for Education and Research (BMBF) and forms part of the GROCE project (Greenland Ice  
430 Sheet/Ocean Interaction) (Grant 03F0778F). We acknowledge the High Performance Computing  
431 Centre (HPC) at the University of Erlangen-Nürnberg's Regional Computation Centre (RRZE), for  
432 their support and resources whilst running the Polar WRF simulations.

433

## 434 **9. References**

435 Banzon, V., Smith, T.M., Chin, T.M., Liu, C. and Hankins, W: A long-term record of blended satellite  
436 and in situ sea-surface temperature for climate monitoring, modelling and environmental studies,  
437 *Earth Syst. Sci. Data*, 8, 165-176. <https://doi.org/10.5194/essd-8-165/2016>, 2016.

438 Bennartz, R., Shupe, M. D., Turner, D. D., Walden, V. P., Steffen, K., Cox, C. J., Kulie, M.S., Miller,  
439 B.B. and Pettersen, C: July 2012 Greenland melt extent enhanced by low-level liquid clouds, *Nature*,  
440 496(7443), 83–86. <https://doi.org/10.1038/nature12002>, 2013.

441 Bowden, J.H., Nolte, C.G. and Otte, T.L: Simulating the impact of the large-scale circulation on the  
442 2-m temperature and precipitation climatology. *Clim. Dyn.*, 40, 1903-1920,  
443 <https://doi.org/10.1007/s00382-012-1440-y>, 2013.

444 Bromwich, D. H., Hines, K. M., and Bai, L: Development and testing of Polar Weather Research and  
445 Forecasting model: 2. Arctic Ocean, *J. of Geophys. Res.*, *114*(D8), D08122.  
446 <https://doi.org/10.1029/2008JD010300>, 2009.

447 Chen, F and Dudhia, J: Coupling an advanced land surface-hydrology model with the Penn State-  
448 NCAR MM5 modeling system. Part 1: Model implementation and sensitivity. *Mon. Weather Rev.*,  
449 *129*, 569-585, [https://doi.org/10.1175/15200493\(2001\)129<0569:CAALSH>2.0.CO;2](https://doi.org/10.1175/15200493(2001)129<0569:CAALSH>2.0.CO;2), 2001.

450 Cho, H., Jun, S-Y., Ho, C-H. and McFarquhar, G: Simulations of winter Arctic clouds and associated  
451 radiation fluxes using different cloud microphysics schemes in the Polar WRF: Comparisons with  
452 CloudSat, CALIPSO and CERES. *JGR:Atmospheres*, *125*(2), e2019JD031413.  
453 <https://doi.org/10.1029/2019JD031413>, 2020.

454 Dee, D. P., Uppala, S. M., Simmons, A. J., Berrisford, P., Poli, P., Kobayashi, S., Andrae, U.,  
455 Balsameda, M.A., Balsamo, G., Bauer, P., Bechtold, P., Beljaars, A.C.M., van de Berg, L., Bidlot,  
456 J., Bormann, N., Delsol, C., Dragani, R., Fuentes, M., Geer, A.J., Haimberger, L., Healy, S.B.,  
457 Hersbach, H., Hólm, E.V., Isaken, L., Kållberg, P., Köhler, M., Matricardi, M., McNally, A.P.,  
458 Monge-Sanz, B.M., Morcrette, J.J., Park, B.K., Peubey, C., de Rosney, P., Tavolato, C., Thépaut,  
459 J.N and Vitart, F: The ERA-Interim reanalysis: configuration and performance of the data  
460 assimilation system. *Quart. J. of the R. Met. Soc.*, *137*(656), 553–597,  
461 <https://doi.org/10.1002/qj.828>, 2011.

462 DuVivier, A. K., and Cassano, J. J: Evaluation of WRF Model Resolution on Simulated Mesoscale  
463 Winds and Surface Fluxes near Greenland. *Mon. Weather Rev.*, *141*(3), 941–963.  
464 <https://doi.org/10.1175/MWR-D-12-00091.1>, 2013.

465 ENVEO: Greenland Calving Front Dataset, 1990-2017, v3.0, Greenland Ice Sheet CCI, from  
466 <http://cryoportals.enveo.at>, 2019.

467 European Space Agency Climate Change Initiative landuse product, available from  
468 <https://www.esalandcover-cci.org/>, last accessed September 5 2019.

469 Fausto, R.S and van As, D: Programme for monitoring of the Greenland ice sheet (PROMICE):  
470 Automatic weather station data. Version: v03, Dataset published via Geological Survey of  
471 Denmark and Greenland. <https://doi.org/10.22008/promice/data/aws>, 2019.

472 Fettweis, X., Box, J. E., Agosta, C., Amory, C., Kittel, C., Lang, C., ... Gallée, H: Reconstructions  
473 of the 1900-2015 Greenland ice sheet surface mass balance using the regional climate MAR model.  
474 *The Cryosphere*, *11*(2), 1015–1033, <https://doi.org/10.5194/tc-11-1015-2017>, 2017.

475 Hines, K. M., and Bromwich, D. H: Development and Testing of Polar Weather Research and  
476 Forecasting (WRF) Model. Part I: Greenland Ice Sheet Meteorology\*, *Mon. Weather Rev.*, *136*(6),  
477 1971–1989, <https://doi.org/10.1175/2007MWR2112.1>, 2008.

478 Hines, K. M., Bromwich, D. H., Bai, L.-S., Barlage, M., Slater, A. G. : Development and Testing  
479 of Polar WRF. Part III: Arctic Land\*, *J. of Climate*, *24*(1), 26–48.

480 <https://doi.org/10.1175/2010JCLI3460.1>, 2011.

481 Hines, K. M., Bromwich, D. H., Bai, L., Bitz, C. M., Powers, J. G., Manning, K. W.: Sea Ice  
482 Enhancements to Polar WRF\*. *Mon. Weather Rev.*, 143(6), 2363-2385.

483 <https://doi.org/10.1175/MWR-D-14-00344.1>, 2015.

484 Hines, K. M., and Bromwich, D. H: Simulation of Late Summer Arctic Clouds during ASCOS with  
485 Polar WRF. *Mon. Weather Rev.*, 145(2), 521–541. <https://doi.org/10.1175/MWR-D-16-0079.1>, 2017.

486 Hochreuther, P, Friedrich Alexander Universtiy, Personal Communication, July 2019.

487 Hong, S.-Y., Noh, Y., Dudhia, J., Hong, S.-Y., Noh, Y., and Dudhia, J: A New Vertical Diffusion  
488 Package with an Explicit Treatment of Entrainment Processes. *Mon. Weather Rev.*, 134(9), 2318–  
489 2341. <https://doi.org/10.1175/MWR3199.1>, 2006.

490 Howat, I. and Eddy, A: Multi-decadal retreat of Greenland’s marine-terminating glaciers. *J. of*  
491 *Glaciology*, 57(203), 389-396. Doi:10.3189/002214311796905631, 2011.

492 Janjić, Z. I: The Step-Mountain Eta Coordinate Model: Further Developments of the Convection,  
493 Viscous Sublayer, and Turbulence Closure Schemes. *Mon. Weather Rev.*,122(5),927–945,  
494 [https://doi.org/10.1175/15200493\(1994\)122<0927:TSMECM>2.0.CO;2](https://doi.org/10.1175/15200493(1994)122<0927:TSMECM>2.0.CO;2), 1994.

495 Joughin, I., Smith, B. E., Howat, I. M., Scambos, T., and Moon, T: Greenland flow variability from  
496 ice-sheet-wide velocity mapping. *Journal of Glaciology*, 56(197), 415–430,  
497 <https://doi.org/10.3189/002214310792447734>, 2010.

498 Kain, J. S: The Kain–Fritsch Convective Parameterization: An Update. *J. of App. Met.*,43(1),  
499 170–181.[https://doi.org/10.1175/1520-0450\(2004\)043<0170:TKCPAU>2.0.CO;2](https://doi.org/10.1175/1520-0450(2004)043<0170:TKCPAU>2.0.CO;2), 2004.

500 Khan, S. A., Kjær, K. H., Bevis, M., Bamber, J. L., Wahr, J., Kjeldsen, K. K., Bjørk, A.A.,  
501 Korsgaard, N.J., Stearns, L.A., van den Broeke, M.R, Liu, L., Larsen, N.K. and Muresan, I. S:  
502 Sustained mass loss of the northeast Greenland ice sheet triggered by regional warming. *Nature*  
503 *Climate Change*, 4(4), 292–299. <https://doi.org/10.1038/nclimate2161>, 2014.

504 Kuipers Munneke, P., Smeets, C. J. P. P., Reijmer, C. H., Oerlemans, J., van de Wal, R. S. W., and  
505 van den Broeke, M. R: The K-transect on the western Greenland Ice Sheet: Surface energy balance  
506 (2003–2016). *Arctic, Antarctic, and Alpine Res.*, 50(1), e1420952.  
507 <https://doi.org/10.1080/15230430.2017.1420952>, 2018.

508 Lachlan-Cope, T., Listowski, C., and O’Shea, S: The microphysics of clouds over the Antarctic  
509 Peninsula - Part 1: Observations, *Atmos. Chem. Phys.*, 16(24), 15605–15617.  
510 <https://doi.org/10.5194/acp-16-15605-2016>, 2016.

511 Larsen, N. K., Levy, L. B., Carlson, A. E., Buizert, C., Olsen, J., Strunk, A., Bjørk, A.A. and Skov,  
512 D. S: Instability of the Northeast Greenland Ice Stream over the last 45,000 years, *Nature Comms*,  
513 9(1), 1872. <https://doi.org/10.1038/s41467-018-04312-7>, 2018.

514 Leeson, A. A., Eastoe, E., and Fettweis, X: Extreme temperature events on Greenland in  
515 observations and the MAR regional climate model, *The Cryosphere*, 12(3), 1091–1102.

516 <https://doi.org/10.5194/tc-12-1091-2018>, 2018.

517 Listowski, C., and Lachlan-Cope, T: The microphysics of clouds over the Antarctic Peninsula Part 2:  
518 modelling aspects within Polar WRF, *Atmos. Chem. Phys.*, 17(17), 10195-10221.  
519 <https://doi.org/10.5194/acp-17-10195-2017>, 2017.

520 Lo, J.C-F., Yang, Z-L. and Pielke Sr, R.A: Assessment of three dynamical climate downscaling  
521 methods using the Weather Research and Forecasting (WRF) model, *JGR: Atmospheres.* 113,  
522 D09112, <https://doi.org/10.1029/2007JD009216>, 2008.

523 Mayer, C., Schaffer, J., Hattermann, T., Floricioiu, D., Krieger, L., Dodd, P. A., Kanzow, T.,  
524 Licciulli, C. and Schannwell, C: Large ice loss variability at Nioghalvfjærdsfjorden Glacier,  
525 Northeast Greenland, *Nature Comms.*, 9(1), 2768. <https://doi.org/10.1038/s41467-018-05180-x>, 2018.

527 Mernild, S. H., Liston, G. E., van As, D., Hasholt, B., and Yde, J. C: High-resolution ice sheet  
528 surface mass-balance and spatiotemporal runoff simulations: Kangerlussuaq, west Greenland,  
529 Arctic, Antarctic, and Alpine Res., 50(1) S100008.  
530 <https://doi.org/10.1080/15230430.2017.1415856>, 2017.

531 Mottram, R., Boberg, F., Langen, P., Yang, S., Rodehacke, C., Christensen, J., and Madsen, M:  
532 Surface mass balance of the Greenland ice sheet in the regional climate model HIRHAM5: Present  
533 state and future prospects, *Low Temp. Sci.*, 75, 105-115, 2017a.

534 Mottram, R., Nielsen, K.P., Gleeson, E., Yang, X: Modelling Glaciers in the HARMONIE-  
535 AROME NWP model, *Adv. Sci. Res.*, 14, 323–334, <https://doi.org/10.5194/asr-14-323-2017>,  
536 2017b.

537 Mouginot, J., Rignot, E., Scheuchl, B., Fenty, I., Khazendar, A., Morlighem, M., Buzzi, A. and  
538 Paden, J: Fast retreat of Zachariæ Isstrøm, northeast Greenland. *Science*, 350(6266), 1357-1361,  
539 <https://doi.org/10.1126/SCIENCE.AAC7111>, 2015.

540 Münchow, A., Schaffer, J. and Kanzow, T: Ocean circulation connecting Fram Strait to Glaciers off  
541 North-East Greenland: Mean flows, topographic Rossby waves, and their forcing. *J. Phys.*  
542 *Oceanography*, 50, 509-530, <https://doi.org/10.1175/JPO-D-19-0085.1>, 2020.

543 Niwano, M., Aoki, T., Hashimoto, A., Matoba, S., Yamaguchi, S., Tanikawa, T., Fujita, K.,  
544 Tsushima, A., Iizuka, Y., Shimada, R., and Hori, M: NHM–SMAP: spatially and temporally high  
545 resolution nonhydrostatic atmospheric model coupled with detailed snow process model for  
546 Greenland Ice Sheet, *The Cryosphere*, 12, 635–655, <https://doi.org/10.5194/tc-12-635-2018>, 2018.

547 Noël, B., van de Berg, W. J., Machguth, H., Lhermitte, S., Howat, I., Fettweis, X., and van den  
548 Broeke, M. R: A daily, 1 km resolution data set of downscaled Greenland ice sheet surface mass  
549 balance (1958–2015). *The Cryosphere*, 10(5), 2361–2377, [https://doi.org/10.5194/tc-10-2361-](https://doi.org/10.5194/tc-10-2361-2016)  
550 [2016](https://doi.org/10.5194/tc-10-2361-2016), 2016.

551 Otte, T.L., Nolte, C.G., Otte, M.J. and Bowden, J.H: Does Nudging Squelch the Extremes in

552 Regional climate modeling? *J. of Climate*, 25, 7046-7066, <https://doi.org/10.1175/JCLID-12->  
553 00048.1, 2012.

554 Pal, S., Change, H-I., Castro, C.L. and Dominguez, F: Credibility of convection-permitting  
555 modeling to improve seasonal precipitation forecasting in the southwestern United States.  
556 *Frontiers Earth Sci.*, 7, 11. <https://doi.org/10.3389/feart.2019.00011>, 2019.

557 Pedersen, S.H., Tamstorf, M.P., Abermann, J., Westergaard-Nielsen, A., Lund, M., Skov, K.,  
558 Sigsgaard, C., Mylius, M.R., Hansen, B.U., Liston, G.E. and Schmidt, N.M: Spatiotemporal  
559 characteristics of seasonal snow cover in Northeast Greenland from in situ observations. *Arctic*,  
560 *Antarctic and Alpine Res.*, 48 (4), 653-671. <https://doi.org/10.1657/AAAR0016-028>, 2016.

561 Polar Weather Research and Forecasting Model, developed by Ohio State University, available  
562 from: <http://polarmet.osu.edu/PWRF/>, last accessed: July 29 2019.

563 Powers, J. G., Klemp, J. B., Skamarock, W. C., Davis, C. A., Dudhia, J., Gill, D. O., Coen, J.L.  
564 and Duda, M. G: The Weather Research and Forecasting Model: Overview, System Efforts, and  
565 Future Directions, *Bull. American Met. Soc.*, 98(8), 1717–1737. <https://doi.org/10.1175/BAMS->  
566 [D-15-00308.1](https://doi.org/10.1175/BAMS-D-15-00308.1), 2017.

567 Rignot, E., Fenty, I., Xu, Y., Cai, C., and Kemp, C: Undercutting of marine-terminating glaciers in  
568 West Greenland, *Geophys. Res. Letters*, 42(14), 5909–5917, <https://doi.org/10.1002/2015GL064236>,  
569 2015.

570 Schaffer, J., von Appen, W.-J., Dodd, P. A., Hofstede, C., Mayer, C., de Steur, L., and Kanzow,  
571 T: Warm water pathways toward Nioghalvfjærdsfjorden Glacier, Northeast Greenland, *J. Geophys.*  
572 *Res: Oceans*, 122(5), 4004–4020, <https://doi.org/10.1002/2016JC012462>, 2017a.

573 Sea Surface Temperature and Sea Ice Concentration Data, available from  
574 <https://rda.ucar.edu/datasets/ds277.7/>, last accessed July 29 2019, doi:10.5065/EMOT-ID34

575 Shepherd, A., et al. : Mass balance of the Greenland Ice Sheet from 1992 to 2018, *Nature*, 579, 233-  
576 239, <https://doi.org/10.1038/s41586-019-1855-2>, 2020.

577 Skamarock, W. C., and Klemp, J. B: A time-split nonhydrostatic atmospheric model for weather  
578 research and forecasting applications. *J. Computational Phys*, 227(7), 3465–3485.  
579 <https://doi.org/10.1016/j.jcp.2007.01.037>, 2008.

580 Tedesco, M., Fettweis, X., Mote, T., Wahr, J., Alexander, P., Box, J. E., and Wouters, B: Evidence  
581 and analysis of 2012 Greenland records from spaceborne observations, a regional climate model  
582 and reanalysis data, *The Cryosphere*, 7(2), 615–630, <https://doi.org/10.5194/tc-7-615-2013>, 2013.

583 Turton, J. V., Mölg, T. & Van As, D: Atmospheric Processes and Climatological Characteristics  
584 of the 79N Glacier (Northeast Greenland), *Mon. Weather Rev.*, 147(4), 1375–1394.  
585 <https://doi.org/10.1175/MWR-D-18-0366.1>, 2019a.

586 Turton, J. V., Mölg, T and Collier, E: NEGIS\_WRF model output, Open Science Framework  
587 Repository, last accessed October 1 2019, doi: /10.17605/OSF.IO/53E6Z, 2019b.

588 Van As, D., Boggild, C.E., Nielsen, S., Ahlstrom, A.P., Fausto, R.S., Podlech, S. and Andersen, M.L:  
589 Climatology and ablation at the South Greenland ice sheet margin from automatic weather station  
590 observations. *The Cryosphere Discussions*, 3, 117-158, <https://doi.org/10.5194/tcd-3-117-2009>, 2009.  
591 van As, D., & Fausto, R: Programme for Monitoring of the Greenland Ice Sheet (PROMICE): first  
592 temperature and ablation records. *Geolog. Survey Denmark Greenland Bulletin*, 23, 73–76, 2011.  
593 van den Broeke, M., Box, J., Fettweis, X., Hanna, E., Noël, B., Tedesco, M., van As, D., van de  
594 Berg, W.J. and van Kampenhout, L: Greenland Ice Sheet Surface Mass Loss: Recent  
595 Developments in Observation and Modeling. *Current Climate Change Rep*, 3(4), 345–356,  
596 <https://doi.org/10.1007/s40641-017-0084-8>, 2017.  
597 Wang, C., Graham, R.M., Wang, K., Gerland, S. and Granskog, M.A: Comparison of ERA5 and  
598 ERA-Interim near surface air temperature, snowfall and precipitation over Arctic sea ice: effects on  
599 sea ice thermodynamics and evolution. *The Cryosphere*, 13, 1661-1679, [https://doi.org/10.5194/tc-](https://doi.org/10.5194/tc-13-1661-2019)  
600 [13-1661-2019](https://doi.org/10.5194/tc-13-1661-2019), 2019.  
601 Weather Research and Forecasting Model, developed by the National Centre for Atmospheric  
602 Research (NCAR). Available from: [https://www.mmm.ucar.edu/weather-research-and](https://www.mmm.ucar.edu/weather-research-and-forecasting-model)  
603 [forecasting-model](https://www.mmm.ucar.edu/weather-research-and-forecasting-model), last accessed: October 1 2019.  
604 Wilson, A. B., Bromwich, D. H., & Hines, K. M: Evaluation of Polar WRF forecasts on the Arctic  
605 System Reanalysis domain: Surface and upper air analysis. *J. Geophys. Res.*, 116(D11), D11112.  
606 <https://doi.org/10.1029/2010JD015013>, 2011.  
607